



# Parametric Symbolic Regression for Discovering Unified Crack Growth Models from Diverse Experiments

Chaoyang Wang,\* Xuan Zhou,<sup>†</sup> Ruizhe Liu,<sup>‡</sup> and Leiting Dong<sup>§</sup>  
*Beihang University, 100191 Beijing, People's Republic of China*

<https://doi.org/10.2514/1.J065701>

Since the introduction of the Paris law, considerable efforts have been devoted to developing more accurate and generalized crack growth models to better support damage tolerance design of aeronautical structures. However, derived mechanism-driven models tend to become increasingly complex as more factors are incorporated, while data-driven models tailored to specific datasets often lack cross-condition generalizability. This study addresses this challenge by introducing a novel parametric symbolic regression (PSR) framework, wherein parametric models share a common mathematical structure with condition-adaptive parameters and are optimized by a multi-objective genetic algorithm guided by multicriteria evaluation metrics. Taking the learning of unified crack growth models for metallic materials as a representative case study, we showcase PSR's capabilities by learning models directly from the Federal Aviation Administration's database, and the discovered model matches the classic NASGRO model's performance with much fewer parameters and enhanced interpretability. Moreover, PSR's efficacy surpasses existing data-driven approaches to discover formulas that accommodate variable experimental conditions and offer high accuracy, interpretability, and parameter stability, highlighting its potential for broader scientific and engineering applications requiring unified models.

## I. Introduction

THE fatigue safety of metallic structures constitutes a critical consideration in the aviation field. Historically, fatigue failures in metal structures have led to numerous catastrophic accidents, such as the structural failures of the Comet and F-111 aircraft [1]. Despite various preventive measures, fatigue-related incidents remained prevalent until the aviation industry introduced "damage tolerance design" and markedly improved the fatigue safety of metal structures. A pivotal milestone in this design philosophy was the introduction of the Paris law [2,3]:

$$\frac{da}{dN} = C(\Delta K)^m \quad (1)$$

In this equation,  $\Delta K$  represents the stress intensity factor range, which drives crack growth;  $da/dN$  denotes the crack growth rate under cyclic fatigue loads; and  $C$  and  $m$  are parameters to reflect material properties and other influencing factors. The Paris law, based on this unified model framework, successfully described crack growth rates observed across multiple experiments, highlighting the inherent similarities in complex crack growth behavior under fatigue loads. This discovery has significantly advanced crack growth analysis methods and facilitated the widespread adoption of the damage tolerance design philosophy.

Despite its foundational importance, the Paris law has inherent limitations as a linear model in double-logarithmic coordinates, and

its parameters  $C$  and  $m$  are insufficient to account for the factors influencing crack growth, such as loading and environmental conditions, crack types, and material states [4]. To address these limitations, researchers have developed various modified models that consider multiple crack growth stages [5,6], crack closure effects [7], loading history [8], environmental conditions [9], crack shape [10], and material variations [11]. While these mechanism-driven models have progressively integrated more factors, their complexity has increased significantly. For instance, the widely adopted NASGRO model [12–14] encompasses numerous factors affecting crack growth (see Appendix B), but its formulation is highly intricate and includes several parameters with undefined physical meanings.

The escalating complexity of crack growth mathematical models poses two major challenges for researchers and engineers. First, comprehensively understanding and mastering these models becomes increasingly difficult, hindering efforts to enhance their generalizability. Second, identifying and prioritizing key features within the models is challenging, complicating their adaptation to specific engineering requirements. To address these challenges, data-driven approaches offer a promising alternative for model development. These approaches enable the creation of data-adaptive models without requiring an in-depth understanding of the underlying physical mechanisms, instead selecting simplified forms based on data characteristics. In recent years, numerous studies have demonstrated the remarkable ability to derive accurate models directly from data [15–19]. Additionally, research has focused on developing new models by learning from generated or experimentally obtained data. These data-driven models have significantly advanced various fields, including the design of new materials [20], the discovery of novel mechanisms [21–23], and the analysis of engineering problems involving diverse mechanical responses in solids and fluids [24–28].

However, existing data-driven modeling approaches do not specifically aim to develop unified models akin to the Paris law. Instead, most methods focus on creating specific models tailored to characterize all training data. For example,

$$\frac{da}{dN} = 4.9 \times 10^{-9} (\Delta K - 2.03)^{3.12} \quad (2)$$

After learning, the constants in the obtained equation are abstracted into parameters such as  $C$ ,  $m$ , and  $\Delta K_{th}$  to form a unified model:

$$\frac{da}{dN} = C(\Delta K - \Delta K_{th})^m \quad (3)$$

Received 2 April 2025; accepted for publication 10 May 2025; published online 8 August 2025. Copyright © 2025 by Authors. Published by the American Institute of Aeronautics and Astronautics, Inc., with permission. All requests for copying and permission to reprint should be submitted to CCC at [www.copyright.com](http://www.copyright.com); employ the eISSN 1533-385X to initiate your request. See also AIAA Rights and Permissions <https://aiaa.org/publications/publish-with-aiaas/rights-and-permissions/>. This work is dedicated to Prof. Zhentong Gao, the pioneer and founding figure of aircraft structural fatigue and reliability research in China, who passed away on January 21, 2025.

\*Ph.D. Candidate, School of Aeronautic Science and Engineering; also Tianmushan Laboratory, 310023 Hangzhou, People's Republic of China.

<sup>†</sup>Assistant Professor, School of Aeronautic Science and Engineering; zhoux@buaa.edu.cn (Co-Corresponding Author).

<sup>‡</sup>Graduate Student, School of Aeronautic Science and Engineering.

<sup>§</sup>Professor & Chairman of School Council, School of Aeronautic Science and Engineering; also Tianmushan Laboratory, 310023 Hangzhou, People's Republic of China; ltdong@buaa.edu.cn (Corresponding Author).

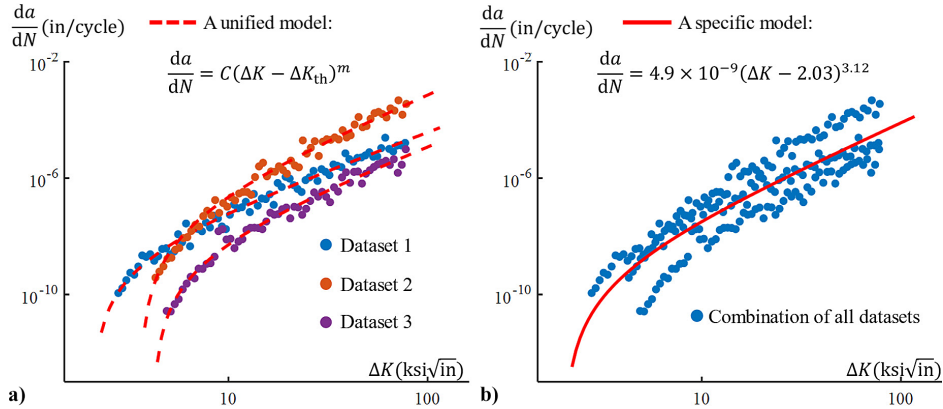


**Fig. 1** a) Representing different datasets using a unified model structure with parameter variations. b) Combining all datasets and modeling them with a specific model.

This approach of deriving unified models has several shortcomings. First, each candidate model is specific, meaning that it fits the entire dataset using a single curve or surface (Fig. 1b). This specificity limits the ability to leverage diverse experimental data under varying conditions, hindering a comprehensive assessment of the model's adaptability. Second, the evaluation metrics used during the learning process are tailored to specific models. As a result, these metrics often fail to provide a holistic view of the candidate model's performance as a unified model.

To address these limitations, this study develops a parametric symbolic regression (PSR) framework for directly learning unified models from diverse experimental data encompassing multiple factors and applies it to the construction of crack growth models for metallic materials. The primary contributions of this work are two-fold. First, we propose a symbolic regression framework based on parametric models, which means that the candidate models during the learning process are parametric rather than specific. This strategy allows each candidate model to independently represent different datasets (Fig. 1a), thereby making full use of diverse experimental data to assess the adaptability of the models. Second, we develop multicriteria evaluation metrics tailored to the requirements of unified models. These metrics encompass complexity, fitness, the number of parameters, and the stability of fitted parameters across different datasets. This comprehensive evaluation framework supports the systematic assessment of candidate models' potential as unified models throughout the learning process.

The remainder of this paper is organized as follows: Section II introduces the implementation of the PSR framework for learning the unified crack growth model. Section III validates the proposed PSR framework using synthetic data generated from representative crack growth models. Section IV applies the PSR framework to experimental data to derive a unified crack growth model and compare it with the NASGRO model. Section V conducts a comparative study of the proposed PSR framework and existing approaches for unified model construction, with a focus on demonstrating its enhanced capabilities and benefits. Finally, Sec. VI presents a summary and outlook of the study.

## II. Parametric Symbolic Regression Framework for Learning Unified Crack Growth Models

The unified crack growth model for metallic materials to be learned in this study is defined as an improved form of the Paris law:

$$\frac{da}{dN} = C(\Delta K)^m \cdot G(X) \quad (4)$$

where  $X$  encompasses variables and constants of crack growth models, and  $G(X)$  represents a dimensionless correction term to be learned. The unified model derived through our data-driven approach is expected to possess the following qualities:

**Capturing similarities across datasets.** By utilizing a unified model structure with adaptable parameters, the model can flexibly represent diverse experimental data influenced by various factors, thereby capturing inherent similarities across different datasets.

**Simplicity and stability for generalization.** The model can effectively describe extensive experimental data with a parsimonious structure, minimizing the number of parameters. Additionally, the fitted parameters remain stable across different datasets, facilitating the model's application to new data.

To meet these requirements, the overall PSR framework for learning unified crack growth models is illustrated in Fig. 2. The left side highlights the first major contribution: a symbolic regression process based on parametric models rather than specific models, which includes the generation, evaluation, and evolution of parametric models  $M_1, M_2, \dots, M_S$  (where  $S$  is the number of models in the population). The right side showcases the distinctive aspect of parametric model evaluation, constituting the second major contribution: thoroughly evaluating candidate models as unified models by leveraging diverse experimental data ( $R$  denotes the stress ratio) and applying multiple evaluation criteria ( $\mathcal{L}_{COPM}, \mathcal{L}_{MSE}, \mathcal{L}_{VAR}$ , and  $\mathcal{L}_{PNUM}$ ; see Sec. II.B).

### A. Generating Parametric Models

This section introduces the generation of diverse model instances to construct the parametric model population. Since most crack growth experimental data are represented in logarithmic coordinates, Eq. (4) is transformed into its logarithmic form. In this context, the correction term to the Paris law captures the mapping relationship between  $X$  and  $\log_{10}(G(X))$ . Consequently, the basis function is defined as  $\log_{10}(F_i(X))$ , and the crack growth model to be learned is expressed as a linear combination:

$$\log_{10}\left(\frac{da}{dN}\right) = \sum_i^N f_i \log_{10}(F_i(X)) \quad (5)$$

where  $N$  denotes the number of basis functions in a single model instance, and  $f_1, f_2, \dots, f_N$  are the corresponding weighting parameters (collectively denoted as  $f$ ). To maintain consistency with the Paris law's part in Eq. (4),  $\log_{10}(F_1(X))$  and  $\log_{10}(F_2(X))$  are fixed as 1 and  $\log_{10}(\Delta K)$ , respectively. The coefficients  $C$  and  $m$  are then replaced by  $f_1$  and  $f_2$  to maintain a coherent parameter description. The remaining basis functions  $F_i(X)$  are generated randomly using a genetic algorithm, thereby creating a diversified model population. An example of generating an individual  $F_i(X)$  is presented in Fig. 3.

In Fig. 3, the corresponding equation is equivalently represented as a model tree: blue nodes symbolize operators (randomly assigned functions), and peach nodes symbolize terminators (randomly selected variables or constants). Thus, the choice of operators and terminators directly defines the space of parametric models. In particular, four operators—addition, subtraction, multiplication, and

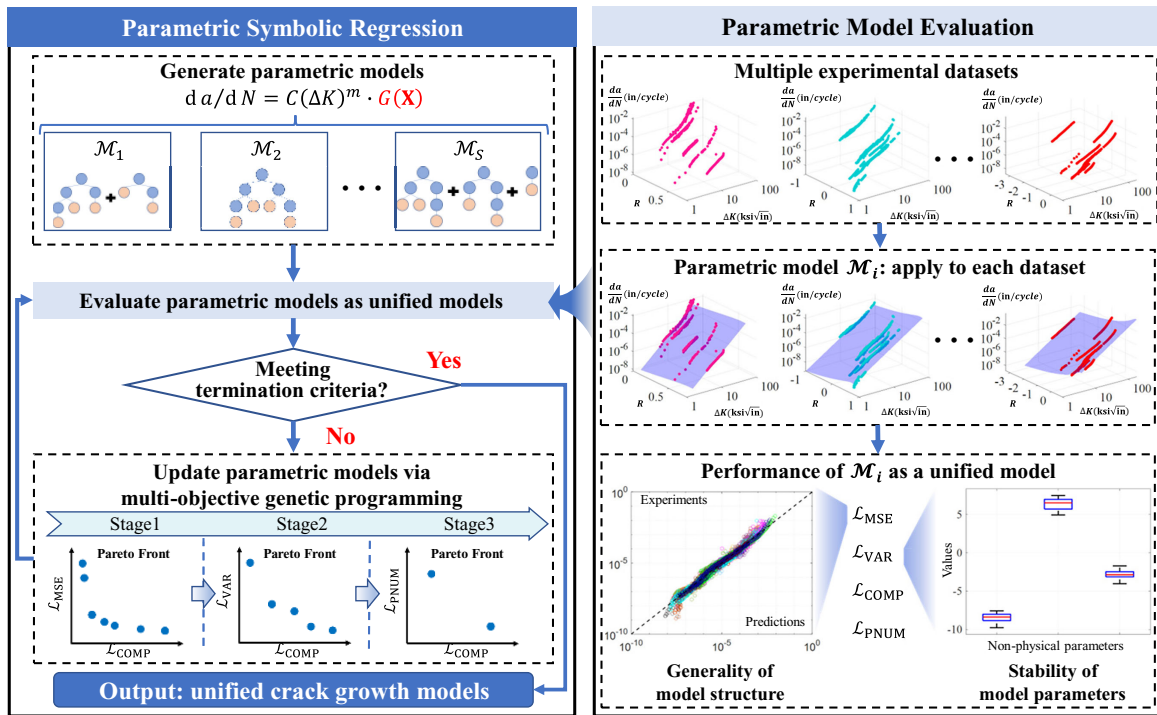


Fig. 2 The parametric symbolic regression framework for discovering unified crack growth models from multiple experimental datasets.

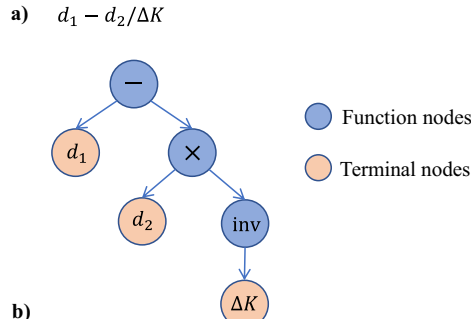


Fig. 3 Representation of the  $F_i(X)$  in a) mathematical expression and b) corresponding tree structure with function and terminal nodes.

inverse operation—are used (Table 1). The inverse operator is included because combining it with multiplication provides a division function while needing only a single input variable. Furthermore, because the basis functions examined here are fixed in logarithmic form, the  $\log_{10}$  operator is not used to construct  $F_i(X)$ .

In addition to these operators, the terminators are defined below.

### 1. Data-Invariant Constants

Data-invariant constants are introduced in the unified model. Specifically, we define  $d_1, d_2, \dots, d_B$  as terminators representing constants in the unified model (collectively denoted as  $\mathbf{d}$ ), where  $B$  is the number of constants in the model. Once values for  $\mathbf{d}$  are assigned, they remain fixed and do not vary across different datasets.

Table 1 Operators used for learning unified crack growth models in this study

Symbol	Meaning	Arguments
+	Add	2
-	Subtract	2
×	Multiply	2
inv	Invert	1

### 2. Input Variables

$\Delta K$  and  $K_{\max}$  are employed as driving forces for crack growth, with  $K_{\max}$  representing the maximum stress intensity factor under cyclic loading. Because  $G(\mathbf{X})$  needs to be dimensionless,  $\Delta K$  and  $K_{\max}$  are nondimensionalized before being used as inputs:

$$\begin{cases} x_1 = \frac{\Delta K}{k_1} \\ x_2 = \frac{K_{\max}}{k_2} \end{cases} \quad (6)$$

where  $k_1$  and  $k_2$  (together denoted as  $\mathbf{k}$ ) share the same dimensional units as the stress intensity factor. These parameters must satisfy

$$\begin{cases} k_1 > 0 \\ k_2 > 0 \end{cases} \quad (7)$$

In summary, the above expressions serve as the foundation for symbolic regression and will be illustrated using several classical crack growth models (Table 2), including the Paris, Walker, Forman, NASGRO (H-S), and NASGRO models. In this paper, we will utilize this straightforward expression as a foundation for developing unified crack growth models that can effectively characterize the diverse experimental data.

### B. Evaluating Parametric Models as Unified Models

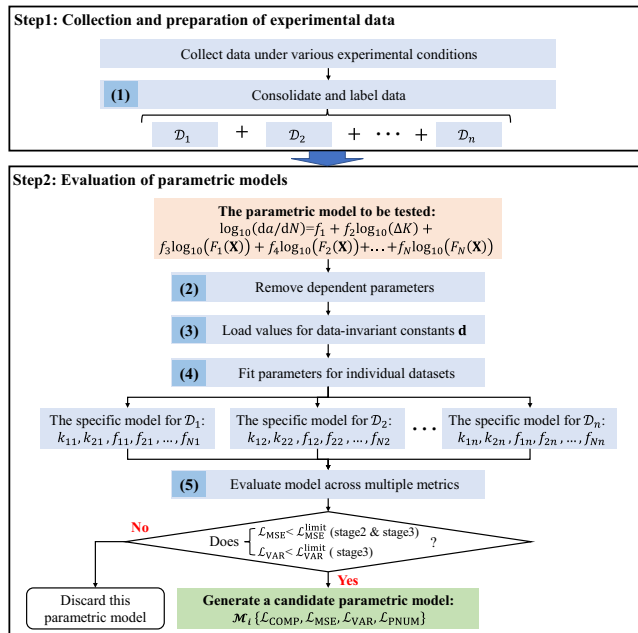
Following the generation of the parametric model population, each candidate will be comprehensively evaluated against the criteria of a unified model. The overall evaluation process is illustrated in Fig. 4.

#### 1. Consolidate and Label Data

In many engineering scenarios, structures can experience variable amplitude loading spectra that cover a wide range of stress ratios. To ensure that models derived from limited stress-ratio datasets meet engineering requirements, data acquired under distinct stress ratios but otherwise identical conditions are assigned a common set of fitting parameters. This allows the resulting parameters to be applied

**Table 2** Typical crack growth models illustrated by the PSR framework

Name	Model	Required $F_i(X)$
Paris	$\frac{da}{dN} = C(\Delta K)^m$	$d_1$
Walker	$\frac{da}{dN} = C(\Delta K)^m(1 - R)^p$	$(x_1 \times \frac{1}{x_2})$
Forman	$\frac{da}{dN} = C(\Delta K)^m \frac{1}{\frac{K_c}{K_{\max}} - 1}$	$(\frac{1}{x_2} - d_1)$
NASGRO	$\frac{da}{dN} = C(\Delta K)^m \left( \frac{1-f}{1-R} \right)^m \frac{\left( 1 - \frac{\Delta K_{\text{thr}}}{\Delta K} \right)^p}{\left( 1 - \frac{K_{\max}}{K_c} \right)^q}$	$(x_1 \times \frac{1}{x_2}), (d_1 - \frac{1}{x_1}), (d_2 - x_2)$
NASGRO (H-S)	$\frac{da}{dN} = C(\Delta K)^m \frac{\left( 1 - \frac{\Delta K_{\text{thr}}}{\Delta K} \right)^m}{\left( 1 - \frac{K_{\max}}{A} \right)^{\frac{m}{2}}}$	$(d_1 - \frac{1}{x_1}), (d_2 - x_2)$

**Fig. 4** Flowchart for parametric model evaluation.

in predicting crack growth across a range of stress ratios. After this consolidation step, the  $n$  labeled datasets  $\{\mathcal{D}_1, \mathcal{D}_2, \dots, \mathcal{D}_n\}$  are employed for model learning.

## 2. Remove Dependent Parameters

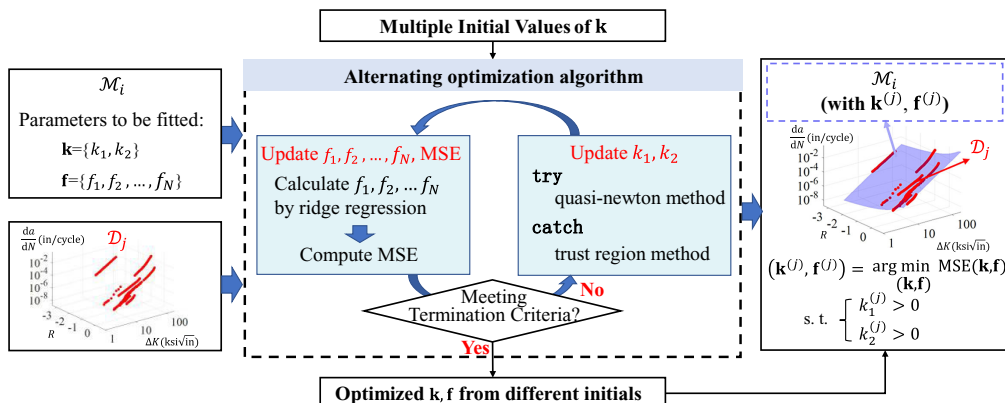
To evaluate the representational capability of a parametric model, it must be fitted to multiple datasets. However, dependent parameters can interfere with model fitting. We therefore check for parameter dependence and remove any redundant parameters. First, we test whether any two basis functions  $F_i(X)$  and  $F_j(X)$  in Eq. (5) can be simplified to the same expression, thereby eliminating linearly dependent basis functions. Next, we verify whether  $G(\pi k_1, \pi k_2)$  and  $G(k_1, k_2)$  reduce to the same form, indicating a proportional correlation between  $k_1$  and  $k_2$ . If so, we set  $k_1 = 1$ .

## 3. Load Values for Data-Invariant Constants $d$

Since  $d_i$  has no physical meaning here and remains fixed once chosen, the sampling space can be defined as  $\{-1, 0, 1\}$ . Additionally, by using the “-” operator, the case  $d_i = 0$  can be written as “1 – 1”, and  $d_i = -1$  as “0 – 1.” Consequently, for the purposes of this study, each constant  $d_i$  is set to 1 when constructing the crack growth models.

## 4. Fit Parameters for Individual Datasets

To compare various parametric models in the population, each model must be reliably fitted to different datasets. We employ an alternating optimization method (Fig. 5) that updates two groups of

**Fig. 5** Model parameter fitting process based on alternating optimization.

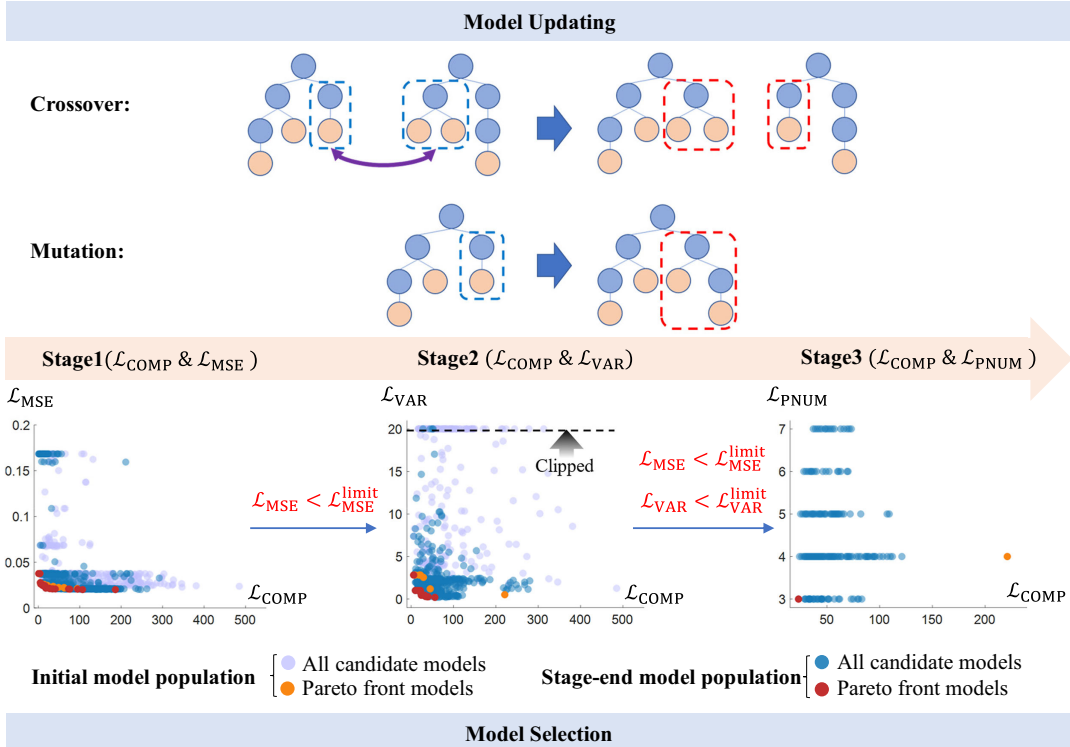


Fig. 6 Evolution of models using genetic programming with a staged selection strategy.

parameters in turn: the parameters  $\mathbf{k}$  are updated through unconstrained nonlinear optimization, while the parameters  $\mathbf{f}$  are updated using the ridge regression. These two steps alternate until the parameters converge to an optimal solution.

To enhance the robustness of this fitting process, multiple initial values for  $\mathbf{k}$  are explored to avoid local optima. Initially, the quasi-Newton method is used for updating  $\mathbf{k}$ . If it fails, the trust region method is employed as a fallback. (The termination criteria used in this paper are shown in Table A1 in Appendix A.) Finally, the parameter set that satisfies the constraints in Eq. (7) and yields the lowest mean squared error (MSE) is selected as optimal, denoted as  $(\mathbf{k}^{(j)}, \mathbf{f}^{(j)})$ .

##### 5. Evaluate the Model Across Multiple Metrics

In the PSR framework, each candidate model is tested on multiple datasets, resulting in several sets of fitted parameters and corresponding MSE values. We employ a multicriteria evaluation scheme to comprehensively assess each candidate's potential as a unified model. The first evaluation metric is complexity, which reflects model interpretability. For each basis function tree  $F_i(\mathbf{X})$ , complexity is defined as the weighted sum of its nodes:

$$\text{COMP}_{F_i(\mathbf{X})} = \sum_{l=1}^h t_l \quad (8)$$

where  $h$  denotes the total number of nodes in the model tree for  $F_i(\mathbf{X})$ , and  $t_l$  denotes the depth of the  $l$ th node. The overall model complexity is then given by

$$\mathcal{L}_{\text{COMP}} = \sum_{i=1}^N \text{COMP}_{F_i(\mathbf{X})} \quad (9)$$

The second metric is fitness, which assesses a model's capacity to represent a broad range of data. We define the fitness of a candidate model as

$$\mathcal{L}_{\text{MSE}} = 1/2 \max (\text{MSE}_1, \text{MSE}_2, \dots, \text{MSE}_n) \quad (10)$$

where  $\text{MSE}_j$  is the mean squared error of the candidate model evaluated on the dataset  $\mathcal{D}_j$ .

The third metric is parameter stability. The learned model should exhibit relatively stable parameter values across different datasets, ensuring the ability of reliable parameter estimates for unseen data. Accordingly, stability is quantified as

$$\mathcal{L}_{\text{VAR}} = \max (\text{var}(\mathbf{f}_1), \text{var}(\mathbf{f}_2), \dots, \text{var}(\mathbf{f}_N)) \quad (11)$$

where  $\mathbf{f}_i = (f_{i1}, f_{i2}, \dots, f_{in})$ , and  $f_{ij}$  is the fitted value of parameter  $f_i$  for the dataset  $\mathcal{D}_j$ . The variance  $\text{var}(\mathbf{f}_i)$  captures how consistently  $f_i$  is estimated across different datasets.

The fourth metric is the number of parameters without physical meaning, defined simply as

$$\mathcal{L}_{\text{PNUM}} = N \quad (12)$$

A model with fewer parameters reduces the complexity of parameter updates, thereby simplifying its broader application.

##### C. Updating Parametric Models via a Multi-Objective Genetic Algorithm

After evaluating the candidate models, a multi-objective genetic algorithm is developed based on Ref. [29] to update the model population to identify superior candidates across multiple metrics. In this framework, each basis function  $F_i(\mathbf{X})$  is treated as a gene, and population members are updated via simulated crossover and mutation events, mirroring biological evolution [30].

Additionally, a staged model selection strategy is introduced to handle multi-objective optimization (Fig. 6). Each stage implements bi-objective optimization while consistently applying  $\mathcal{L}_{\text{COMP}}$  to exclude models with low interpretability. However, the specific criteria vary among stages. In the first stage,  $\mathcal{L}_{\text{MSE}}$  and  $\mathcal{L}_{\text{COMP}}$  are adopted, ensuring that the population retains a wide range of models with strong representational capability. In the second stage,  $\mathcal{L}_{\text{VAR}}$  and  $\mathcal{L}_{\text{COMP}}$  are employed, subject to the constraint  $\mathcal{L}_{\text{MSE}} < \mathcal{L}_{\text{MSE}}^{\text{limit}}$ , further filtering models based on parameter stability. In the third stage,  $\mathcal{L}_{\text{PNUM}}$  and  $\mathcal{L}_{\text{COMP}}$  are used, coupled with the constraints  $\mathcal{L}_{\text{MSE}} < \mathcal{L}_{\text{MSE}}^{\text{limit}}$  and  $\mathcal{L}_{\text{VAR}} < \mathcal{L}_{\text{VAR}}^{\text{limit}}$ , to select the most parsimonious candidate models.

### III. Benchmark Testing with Synthetic Data

#### A. Validation of the PSR Framework on Synthetic Data Without Noise

The PSR framework was first tested to ascertain its ability to recover the correct model from data generated by several classical crack growth models, including the Walker and Forman models, as well as the H-S variant of the NASGRO model, whose elegant simplicity and broad applicability have been demonstrated by the comprehensive work of Jones et al. [31–33]. The parameter values used to generate the synthetic data are listed in Tables A2–A4. As shown in Fig. 7b, by setting the maximum number of basis functions to two and the maximum number of basis function layers to three, the model space was sufficient to encompass the Walker, Forman, and NASGRO (H-S) models. Detailed PSR settings are provided in Table 3.

Using noise-free data generated by the Walker, Forman, or NASGRO (H-S) models (Fig. 7a), the PSR framework selected the model

with the fewest parameters located on the Pareto front of the final generation as the output, denoted as  $\mathcal{M}_{\text{out}}$ :

$$\log_{10} \left( \frac{da}{dN} \right) = f_1 + f_2 \log_{10} (\Delta K) + f_3 \log_{10} \left( \frac{x_2^2}{x_1} \right) \quad (13)$$

$$\log_{10} \left( \frac{da}{dN} \right) = f_1 + f_2 \log_{10} (\Delta K) + f_3 \log_{10} \left( \frac{1}{x_2} - 1 \right) \quad (14)$$

$$\begin{aligned} \log_{10} \left( \frac{da}{dN} \right) = & f_1 + f_2 \log_{10} (\Delta K) + f_3 \log_{10} \left( 1 - \frac{1}{x_1} \right) \\ & + f_4 \log_{10} (1 - x_2) \end{aligned} \quad (15)$$

All three models derived by the PSR framework from synthetic data demonstrate excellent performance in both  $\mathcal{L}_{\text{MSE}}$  and  $\mathcal{L}_{\text{VAR}}$  (Table 4), indicating accurate characterization of the learning data

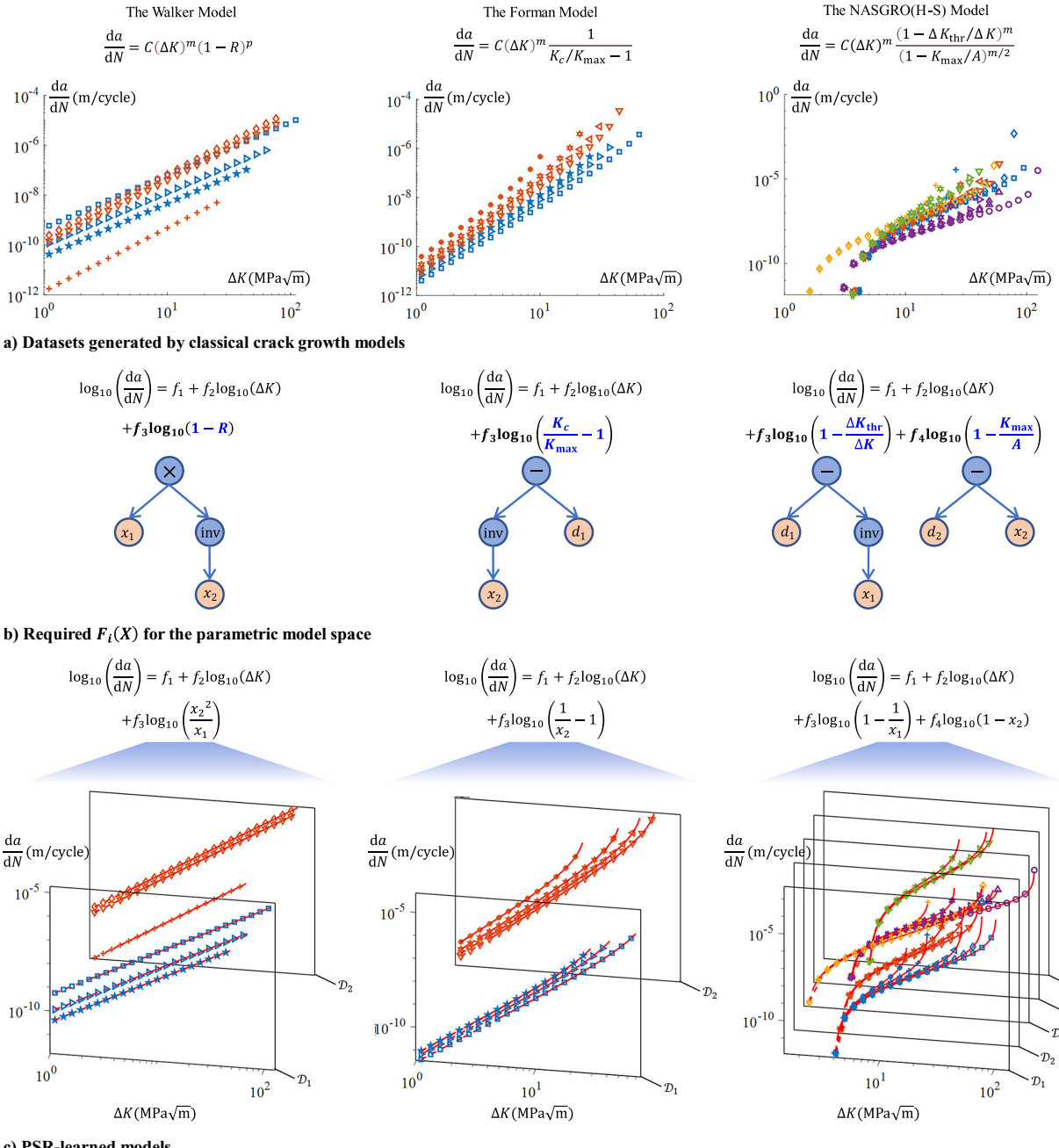


**Table 3** PSR's settings

Symbol	Meaning	Arguments
<i>Settings for genetic programming</i>		
$S$	Number of models in the population	3000
$G_{\max}$	Number of evolutionary generations	60
$S_T$	Sample number for the tournament	100
$g_{\max}^{\text{num}}$	Maximum number of basis functions	2
$\text{depth}_{g_{\max}}$	Maximum number of basis function layers	3
$\text{ERC}_{\max}^{\text{num}}$	Maximum number of constants	2
$P_{\text{mutate}}$	Probability of $F_i(X)$ tree mutation	0.24
$P_{\text{cross}}$	Probability of $F_i(X)$ tree crossover	0.64
$P_{\text{direct}}$	Probability of $F_i(X)$ tree direct copy	0.12
<i>Settings for parameter fitting</i>		
$r$	Ridge regression parameter	0.0
$V_{k_1, k_2}^{\text{ini}}$	Sample space of initial $k_1, k_2$	[1,200]
$S_{k_1, k_2}$	Sample number of initial $k_1, k_2$	10
<i>Settings for the staged screening strategy</i>		
$G_{S1}$	Number of evolutionary generations for stage 1	25
$G_{S2}$	Number of evolutionary generations for stage 2	25
$\mathcal{L}_{\text{MSE}}^{\text{limit}}$	$\mathcal{L}_{\text{MSE}}$ constraint for all models in stages 2 & 3	$10^{-5}$
$\mathcal{L}_{\text{VAR}}^{\text{limit}}$	$\mathcal{L}_{\text{VAR}}$ constraint for all models in stage 3	1.0

**Table 4** Performance of models learned from synthetic data without noise

$M_{\text{out}}$	$\mathcal{L}_{\text{MSE}}$	$\mathcal{L}_{\text{VAR}}$
(13)	$9.6 \times 10^{-29}$	0.68
(14)	$1.3 \times 10^{-11}$	0.088
(15)	$3.8 \times 10^{-13}$	0.079

(Fig. 7c) and stability of the fitted parameters across different datasets.

Indeed, Eqs. (13–15) correspond to the Walker, Forman, and NASGRO (H-S) models used for data generation, as detailed below:

Based on  $\Delta K = (1 - R)K_{\max}$ , Eq. (13) can be transformed into

$$\log_{10} \left( \frac{da}{dN} \right) = \theta_1 + \theta_2 \log_{10} (\Delta K) + \theta_3 \log_{10} (1 - R) \quad (16)$$

where

$$\begin{cases} \theta_1 = f_1 + f_3 \log_{10} \left( \frac{k_1}{k_2^2} \right) \\ \theta_2 = f_2 + f_3 \\ \theta_3 = -2f_3 \end{cases} \quad (17)$$

Thus, Eq. (16) adopts the same form as the Walker model. Similarly, Eqs. (14) and (15) match the Forman and NASGRO (H-S) models, respectively. Furthermore, parameter comparisons in Tables A2–A4 confirm that Eqs. (16), (14), and (15), learned by the PSR framework, are identical to the models used to generate the learning data. Consequently, the PSR framework successfully identified the models from their generated datasets.

## B. Validation of the PSR Framework on Synthetic Data with Noise

To evaluate the learning capability of the PSR framework under noisy conditions, synthetic data were generated by introducing noise into the NASGRO (H-S) model:

**Table 5**  $\mathcal{L}_{\text{MSE}}^{\text{limit}}$  settings for different noise levels controlled by  $\eta$ 

$\eta$	$\mathcal{L}_{\text{MSE}}^{\text{limit}}$
0	$10^{-5}$
0.08	0.006
0.16	0.025
0.24	0.05

**Table 6** Performance of Eq. (15) concerning different noise levels controlled by  $\eta$ 

$\eta$	$\mathcal{L}_{\text{MSE}}$	$\mathcal{L}_{\text{VAR}}$
0	$4.93 \times 10^{-6}$	0.0779
0.08	0.0032	0.0771
0.16	0.0137	0.1141
0.24	0.0311	0.2074

$$\log_{10} \left( \frac{da}{dN} \right)_{\text{noise}} = \log_{10} \left( \frac{da}{dN} \right) + \eta \varepsilon \quad (18)$$

where,  $\varepsilon \sim N(0,1)$  represents the noise term, and  $\eta$  controls the noise variance. We considered four noise levels:  $\eta = 0, 0.08, 0.16, 0.24$  for PSR's testing. Limits for  $\mathcal{L}_{\text{MSE}}$  ( $\mathcal{L}_{\text{MSE}}^{\text{limit}}$ ) were updated as shown in Table 5, and L2 regularization was applied with a ridge regression parameter of  $r = 0.4$  during parameter fitting.

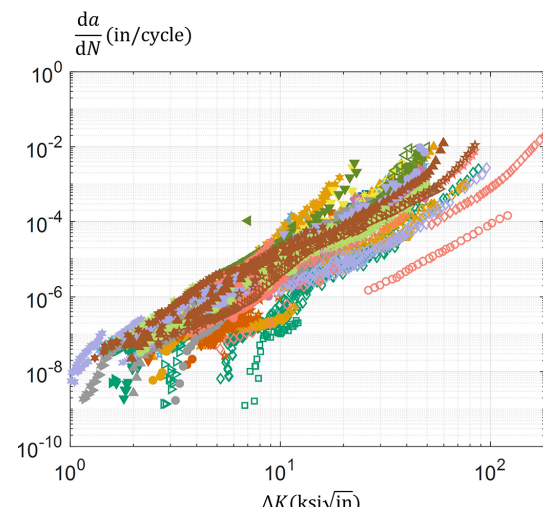
Under all noise levels, the output model  $M_{\text{out}}$  remained consistent with Eq. (15). Its performance across different noise levels is presented in Table 6.

The results demonstrate that the model effectively characterizes the essential features of the data even under high noise levels, indicating that the PSR framework can identify the robust model despite the presence of noise.

## IV. Discovering the Crack Growth Model from Experimental Data

### A. Source of Experimental Data

The experimental data utilized in this study (Fig. 8) were sourced from the database published by the Federal Aviation Administration

**Fig. 8** FAA's database (different colors denote distinct datasets within Table A5, while different symbols indicate varying stress ratios).

(FAA) [34], which encompasses a wide range of experimental data from multiple sources, capturing crack growth performance under various influencing factors such as material forms, heat treatment processes, and experimental environments (Table A5). These factors are highly relevant to engineering applications.

To address the complexity of the experimental data, we adapted PSR's settings used for synthetic data with noise by increasing the population size to 6000, thereby enhancing the diversity of parametric models within the population. After an initial trial of the population evolution in the first stage, we set the  $\mathcal{L}_{\text{MSE}}^{\text{limit}}$  to 0.027.

## B. Analysis of Model Representational Capacity and Parameter Variation Stability Across Different Datasets

After independently running the PSR procedure 10 times on all 13 datasets, we selected the most frequently recurring learned model, hereafter referred to as the ParaGRO model:

$$\log_{10}\left(\frac{da}{dN}\right) = f_1 + f_2 \log_{10}(\Delta K) + f_3 \log_{10} \left[ \frac{\left(\frac{\Delta K}{k_1}\right)^2}{\frac{K_{\max}}{k_2}} + \frac{K_{\max}}{k_2} \right] \quad (19)$$

As illustrated in Fig. 9, experimental data from different sources, influenced by various factors, are effectively characterized by a single model structure, namely the ParaGRO model, with adjustable parameters (Table A6). This demonstrates that the ParaGRO model captures the intrinsic similarities across diverse experimental datasets. Moreover, the ParaGRO model requires only five parameters, which can be reduced to four through artificial merging, as described in Sec. IV.C.

Despite involving fewer parameters than the NASGRO model's 11 varying parameters (Table A7), the ParaGRO model maintains comparable representational capabilities, as shown in Figs. 10a and 10b. This indicates that the ParaGRO model, derived directly from experimental data, effectively captures and exploits the most essential features that reflect the data's intrinsic properties.

Figure 11a displays the boxplots of the fitted nonphysical parameters for the ParaGRO model across different datasets, whereas Fig. 11b shows the boxplots of the NASGRO model's parameters, which lack physical meaning. These plots illustrate the stable parameter variations when applying the ParaGRO model versus the NASGRO model across different datasets. This stability is beneficial for the application of these models to new data, as it ensures reliable reference parameter values can be obtained.

Based on the above analysis, the ParaGRO model directly learned via the PSR framework exhibits fewer parameters and demonstrates stable and reliable parameter variations across different datasets. These attributes make the model particularly suitable for applications such as the airframe digital twin [35], where frequent parameter updates are required.

## C. Interpretability of the PSR-Learned ParaGRO Model

Data-driven models can also offer significant interpretability. We further analyze the ParaGRO model by transforming it using  $\Delta K = (1 - R)K_{\max}$ :

$$\begin{aligned} \log_{10}\left(\frac{da}{dN}\right) &= f_1 - f_3 \log_{10}(k_1) + (f_2 + f_3) \log_{10}(\Delta K) \\ &\quad + f_3 \log_{10} \left[ (1 - R) \frac{k_2}{k_1} + \frac{1}{1 - R} \frac{k_1}{k_2} \right] \end{aligned} \quad (20)$$

thereby

$$\begin{aligned} \frac{da}{dN} &= \\ 10^{f_1 - f_3 \log_{10}(k_1)} &\left\{ \left[ (1 - R) \frac{k_2}{k_1} + \frac{1}{1 - R} \frac{k_1}{k_2} \right] \frac{f_3}{f_2 + f_3} \Delta K \right\}^{(f_2 + f_3)} \end{aligned} \quad (21)$$

Referencing Eq. (16), the above equation can be written as

$$\frac{da}{dN} = \theta_1 \left\{ \left[ (1 - R) \theta_2 + \frac{1}{(1 - R) \theta_2} \right]^{\theta_3} \Delta K \right\}^{\theta_4} \quad (22)$$

where

$$\begin{cases} \theta_1 = 10^{f_1 - f_3 \log_{10}(k_1)} \\ \theta_2 = \frac{k_2}{k_1} \\ \theta_3 = \frac{f_3}{f_2 + f_3} \\ \theta_4 = f_2 + f_3 \end{cases} \quad (23)$$

Thus, the ParaGRO model effectively depends on only four parameters. Building on Elber's model [7], which accounts for crack closure effects, we consider

$$\frac{da}{dN} = C(\Delta K_{\text{eff}})^m \quad (24)$$

$$U = \frac{\Delta K_{\text{eff}}}{\Delta K} = \frac{\Delta S_{\text{eff}}}{\Delta S} \quad (25)$$

where  $\Delta K_{\text{eff}}$  is the effective stress intensity factor range considering crack closure,  $\Delta S$  is the stress range of cyclic loading, and  $\Delta S_{\text{eff}}$  is the effective stress range under crack closure conditions. Therefore, the coefficient preceding  $\Delta K$  in Eq. (22) corresponds to  $U$ :

$$U = \left[ (1 - R) \theta_2 + \frac{1}{(1 - R) \theta_2} \right]^{\theta_3} \quad (26)$$

Consequently, the ratio of crack opening stress to maximum stress is

$$\frac{S_o}{S_{\max}} = 1 - \frac{U \Delta S}{S_{\max}} = 1 - U(1 - R) \quad (27)$$

Figure 12a illustrates the correlation between the nominal crack opening stress  $S_o/S_{\max}$  and the stress ratio  $R$  across 13 datasets, where the various curves, as characterized by Eq. (22), objectively reflect the differences in crack closure behavior among the individual datasets. In comparison, Fig. 12b depicts the corresponding relationship  $f$  from the NASGRO model (Appendix B), in which the crack closure behavior was subjectively set to be identical for all 13 datasets, as represented by the red curve defined in Ref. [34] (the NASGRO model typically adjusts  $f$  by modifying  $\alpha$  or  $S_{\max}/\sigma_0$ , indicated by the black dashed line in Fig. 12b). Our results indicate that the ParaGRO model effectively captures the variation in  $S_o/S_{\max}$  with changes in  $R$ : as the stress ratio decreases, the influence of crack closure intensifies. Moreover, compared to the various formulations developed by Schijve et al. [11] to account for crack growth closure effects in different materials, the ParaGRO model accommodates these differences within a single framework by simply adjusting two parameters  $k_1$  and  $k_2$ .

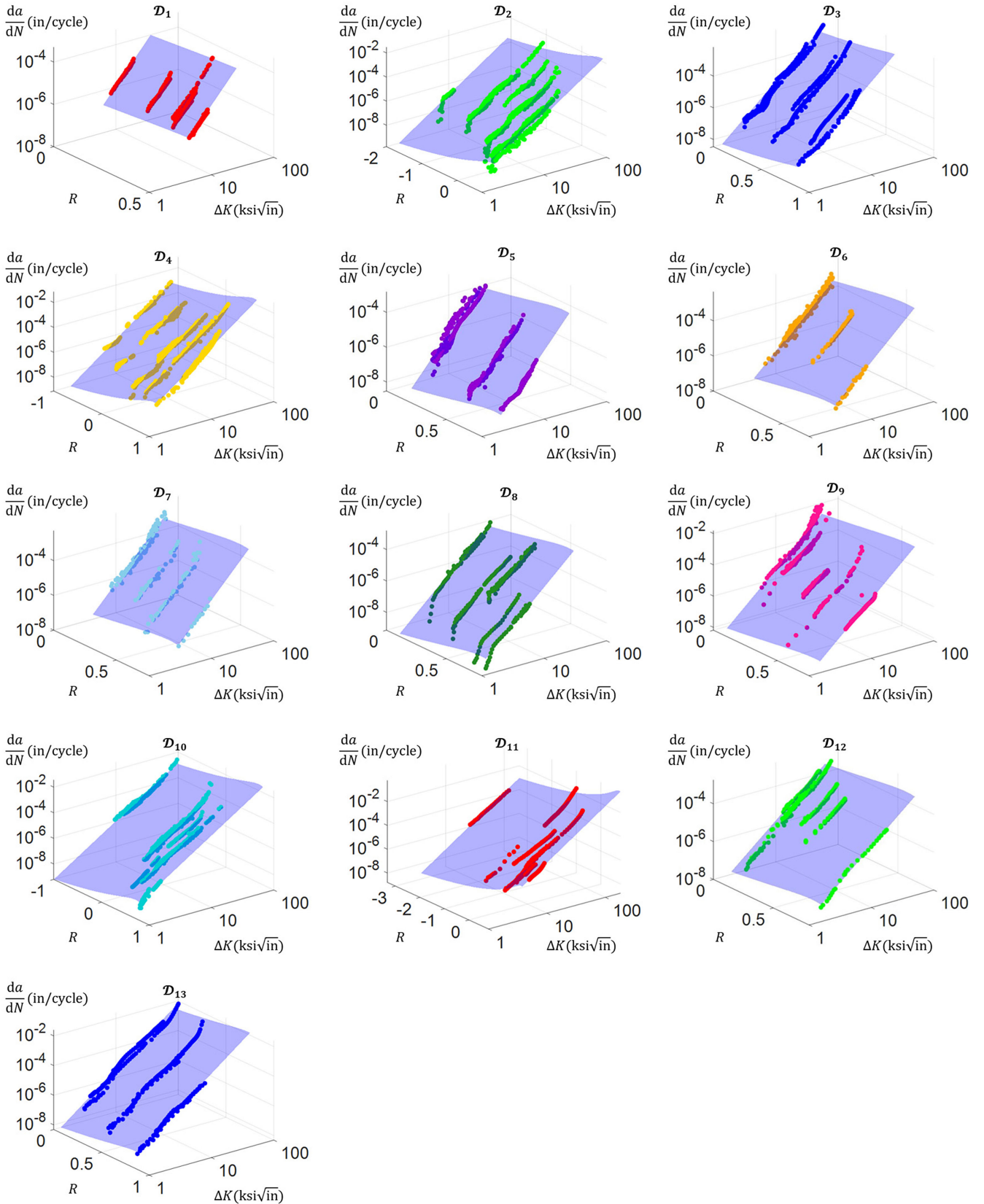


Fig. 9 Characterizing 13 datasets by the ParaGRO model.

## V. Discussion

Most data-driven studies focus on identifying a specific model that fits the entire learning dataset. Typically, a unified model is parameterized from the learned specific model only after the learning phase is complete. Existing methods generally fall into

two categories: the homogeneous-data approach, which utilizes experimental data under similar conditions, and the aggregated-data approach, which combines multiple datasets from varying conditions without addressing differences in influencing factors. This section highlights the advantages of the PSR framework by

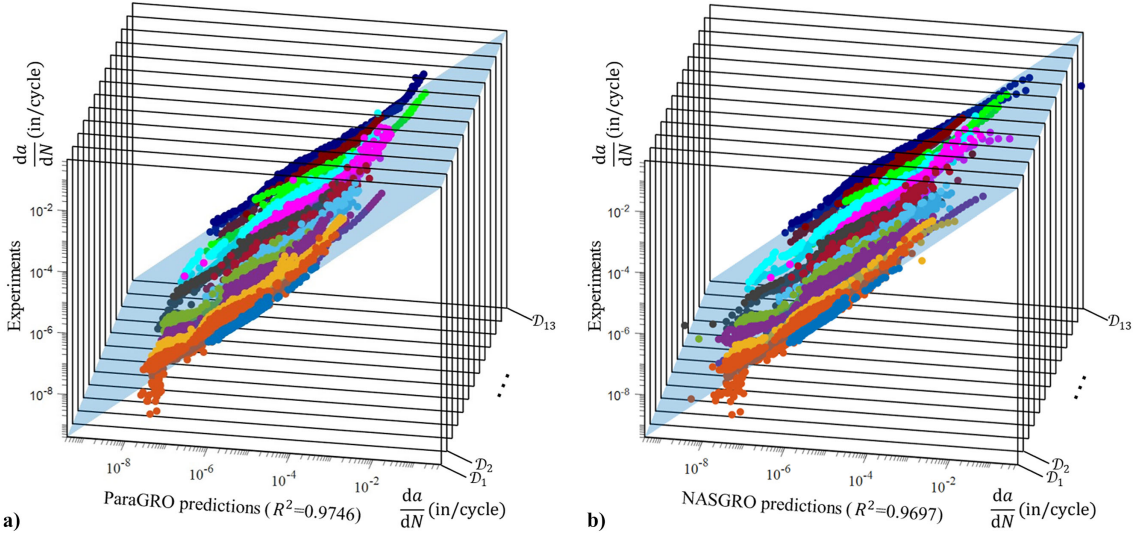


Fig. 10 Predicted versus experimental crack growth rates for 13 datasets: a) ParaGRO and b) NASGRO. Colors denote individual datasets.

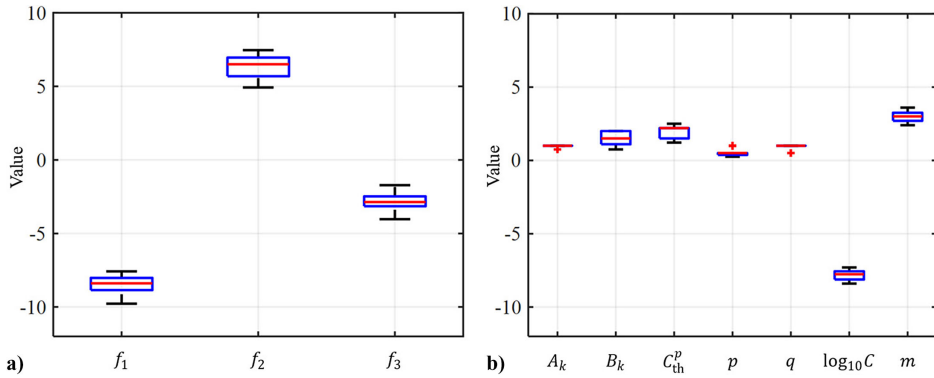


Fig. 11 Boxplots of fitted nonphysical parameters: a) ParaGRO and b) NASGRO. Details of parameters for the NASGRO model are provided in Table A6.

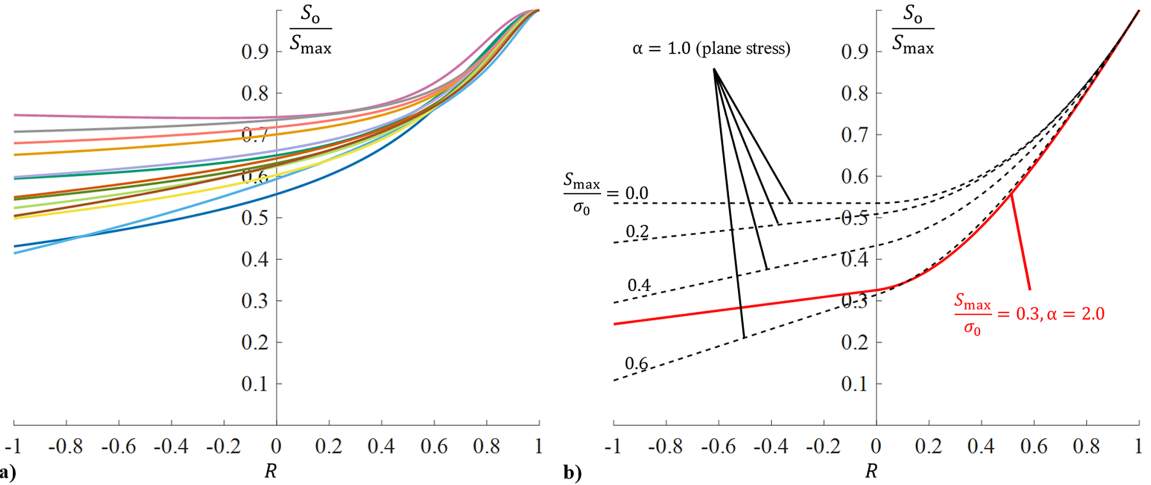


Fig. 12 Normalized crack opening stress  $S_o/S_{\max}$  versus stress ratio  $R$ : a) ParaGRO (colors denote individual datasets); b) NASGRO (the red line).

comparing it with these two approaches in developing unified models.

#### A. Comparison of the PSR Framework with the Homogeneous-Data Approach

Models trained on homogeneous data typically perform well on their training sets but may exhibit poor generalization to new data. In contrast, the PSR framework utilizes parametric models during learning and evaluates each candidate as a unified model across diverse

datasets with varying influencing factors. This strategy effectively enhances the generalization capability of the learned model.

To emulate the homogeneous-data approach, we utilized the symbolic regression process developed in this study alongside the experimental data presented in Table A5. Each dataset was individually selected to train a specific model, which was subsequently transformed into a unified model and evaluated on the remaining 12 datasets. For comparison, the model with the lowest  $\mathcal{L}_{MSE}$  on the learning dataset  $\mathcal{D}_i$  at the 25th generation (end of the first stage) was

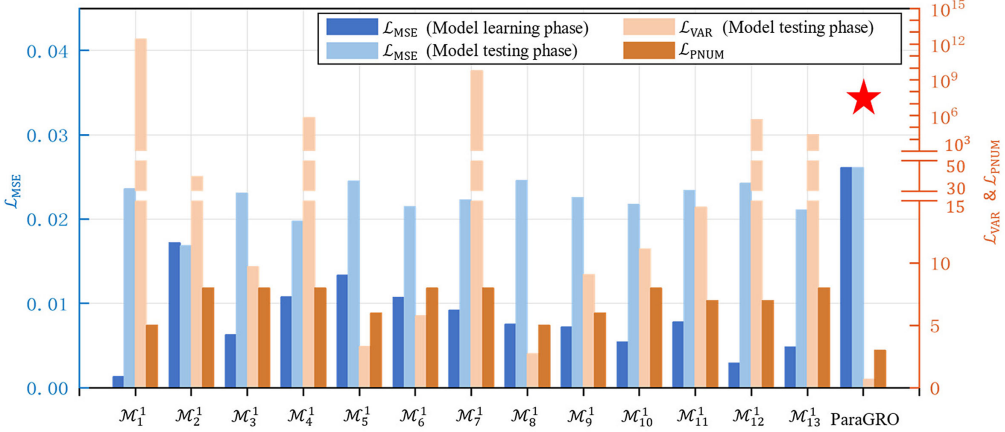


Fig. 13 Comparative performance of the ParaGRO model (learned from all thirteen datasets) versus  $M_i^1$  (learned from a single dataset  $\mathcal{D}_i$ ).

Table 7 Scenarios for learning and testing data division

Data case	Datasets division	
	Learning	Testing
I	$[\mathcal{D}_1:\mathcal{D}_{10}]$	$[\mathcal{D}_{11}:\mathcal{D}_{13}]$
II	$[\mathcal{D}_4:\mathcal{D}_{13}]$	$[\mathcal{D}_1:\mathcal{D}_3]$

identified as the optimal output and parameterized as the unified model  $M_i^1$ . The comparison between them and the ParaGRO model is shown in Fig. 13.

Figure 13 illustrates that models  $M_1^1$  to  $M_{13}^1$  perform well on their respective learning datasets but exhibit significantly higher  $L_{MSE}$  and unstable parameter variations ( $L_{VAR}$ ) on test data. This behavior indicates overfitting and limited generalization when these models are used as unified models. In contrast, the PSR framework

evaluates candidate models across multiple datasets during the learning phase, thereby enhancing the generalization capability of the ParaGRO model. Furthermore, the PSR framework allows for the expansion of training datasets, allowing the PSR-learned model to achieve improved generalization to new datasets by incorporating additional data during the learning phase.

### B. Comparison of the PSR Framework with the Aggregated-Data Approach

Maximizing the utilization of available data to improve model generalization is a widely adopted strategy in machine learning. However, while utilizing extensive experimental datasets, the aggregated-data approach combines them into a single training set and employs a single model to characterize all data. In contrast, the PSR framework utilizes candidate models, each of which shares a unified model structure but adapts its parameters in response to varying influencing factors across different datasets, making it more suitable for representing multiple datasets. This section compares these two data utilization approaches as follows.

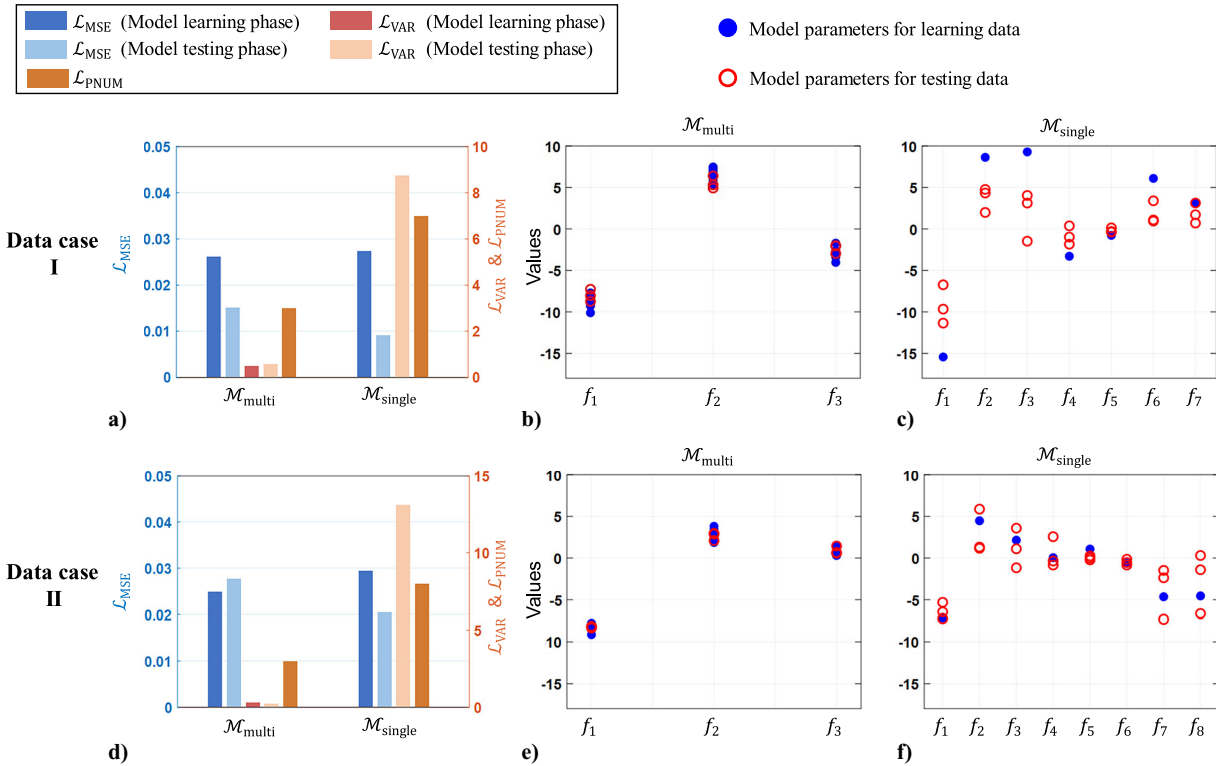


Fig. 14 Comparison of  $M_{multi}$  versus  $M_{single}$  for cases I (a–c) and II (d–f): a,d) evaluation metrics; b,c,e,f) parameters.

To simulate the aggregated-data approach, we utilized the symbolic regression process established in this study along with the experimental data presented in Table A5. Ten datasets were used during the learning phase of the PSR framework, resulting in an output model denoted as  $\mathcal{M}_{\text{multi}}$ . Correspondingly, the same 10 datasets were merged into a single training set to represent the direct aggregation of multiple datasets. The model with the lowest  $\mathcal{L}_{\text{MSE}}$  at the 25th generation (end of the first stage) was selected as the optimal output and parameterized to a unified model, referred to as  $\mathcal{M}_{\text{single}}$ . Both  $\mathcal{M}_{\text{multi}}$  and  $\mathcal{M}_{\text{single}}$  were subsequently tested on three additional datasets to evaluate their performance as unified models. Overall, this section examines two scenarios for dataset division during the model learning and testing phases, as detailed in Table 7.

Results in Figs. 14a and 14d show that during the learning phase,  $\mathcal{M}_{\text{single}}$  exhibits a higher  $\mathcal{L}_{\text{MSE}}$  despite having more parameters than  $\mathcal{M}_{\text{multi}}$  across both data cases. This indicates that directly merging multiple datasets into a single training set does not facilitate the learning of a more parsimonious and accurate model when experimental data exhibit significant dispersion due to varying influencing factors. In the testing phase,  $\mathcal{M}_{\text{multi}}$  demonstrates a slightly higher  $\mathcal{L}_{\text{MSE}}$  than  $\mathcal{M}_{\text{single}}$  but with significantly fewer parameters. More importantly,  $\mathcal{M}_{\text{multi}}$  shows better stability in parameter fitting across different datasets (Figs. 14b and 14e vs Figs. 14c and 14f), and its parameters on the testing set are closer to those of the learning set compared to  $\mathcal{M}_{\text{single}}$ . This suggests better engineering practicality, as the parameter values obtained during learning can serve as reliable references when using  $\mathcal{M}_{\text{multi}}$  for new data.

## VI. Conclusions

This study proposes a novel PSR framework for learning unified models from diverse datasets. Its effectiveness is demonstrated through the construction of crack growth models for metallic materials. The PSR framework can leverage extensive experimental data encompassing multiple influencing factors to derive a unified crack growth model that is simple, well-generalized, and stable.

The PSR framework distinguishes itself from traditional data-driven approaches in two key aspects. First, unlike conventional methods that rely on specific models, the PSR framework employs parametric models within the symbolic regression process. These candidate models incorporate both variables and

parameters, enabling their evolution and evaluation in a manner analogous to the conventional derivation of formulas. This approach allows the PSR framework to capture the intrinsic similarities across diverse datasets while maintaining flexibility in parameter adaptation. Second, we established multicriteria evaluation metrics specifically tailored to the requirements of unified models. These metrics consider complexity, fitness, the number of parameters, and the stability of fitted parameters across different datasets. This comprehensive evaluation framework ensures that each candidate model fully utilizes the diverse experimental data, enabling a thorough assessment of its performance as a unified model during the symbolic regression process.

When tested using the FAA-released database, the PSR-generated crack growth model demonstrated characterization capabilities comparable to the classical NASGRO model, which utilizes 11 parameters. Notably, our model achieved similar performance with only four parameters, significantly reducing complexity while maintaining high accuracy. Furthermore, the PSR-derived model effectively captures crack closure effects, offering enhanced interpretability compared to the NASGRO model. The advantages of the PSR framework extend beyond its ability to generate accurate and interpretable models. By evaluating candidate models across multiple datasets with varying influencing factors, the PSR framework significantly enhances the generalization and stability of the resulting unified model. This capability is particularly valuable in engineering applications, where reliable and adaptable models are essential for predicting material behavior under diverse conditions.

The PSR framework holds substantial potential for application in various fields. Its ability to derive unified models from diverse datasets makes it a powerful tool for uncovering underlying physical mechanisms and developing mechanism-driven models. Future work will explore the application of the PSR framework in learning material mechanical behaviors, uncovering flow mechanisms, and addressing other complex scientific and engineering challenges.

In conclusion, the PSR framework represents a significant advancement in data-driven modeling, offering a robust framework for constructing simple, interpretable, and well-generalized models. Its success in crack growth modeling underscores its potential to transform data-driven approaches across a wide range of disciplines.

## Appendix A: Supplementary Tables

**Table A1 Termination criteria for nonlinear optimization algorithms**

Symbol	Meaning	Arguments	
		The quasi-Newton method	The trust region method
$\epsilon_{\text{opt}}$	Gradient tolerance ( $\ \nabla \text{MSE}(k_1, k_2)\ _\infty$ )	$10^{-6}$	$10^{-10}$
$\epsilon_{\text{MSE}}$	Function tolerance (MSE)	$10^{-6}$	$10^{-10}$
$\epsilon_{\text{step}}$	Step tolerance	$10^{-10}$	$10^{-10}$
$P_{\max}$	Max iterations	400	2000

**Table A2 Parameters for data generation using the Walker model and fitting parameters of Eq. (16)**

Data label	Parameters of Walker				Parameters of model				
	R	p	C	m	$k_1$	$k_2$	$10^{\theta_1}$	$\theta_2$	$\theta_3$
1	-0.2, 0.3, 0.5	3.0	$2.79 \times 10^{-10}$	2.12	1.00	1.00	$2.79 \times 10^{-10}$	2.12	3.00
2	0.1, 0.2, 0.7	4.5	$3.12 \times 10^{-10}$	2.54	1.00	1.00	$3.12 \times 10^{-10}$	2.54	4.50

**Table A3** Parameters for data generation using the Forman model and fitting parameters of Eq. (14)

Data label	$R$	Parameters of Forman			Parameters of model				
		$K_c$	$C$	$m$	$k_1$	$k_2$	$10^{f_1}$	$f_2$	$f_3$
1	-0.2, 0.3, 0.5	79	$2.79 \times 10^{-10}$	2.12	1.00	79.00	$2.79 \times 10^{-10}$	2.12	-1.00
2	0.2, 0.4, 0.6, 0.8	62	$3.12 \times 10^{-10}$	2.54	1.00	62.00	$3.12 \times 10^{-10}$	2.54	-1.00

**Table A4** Parameters for data generation using the NASGRO (H-S) model and fitting parameters of Eq. (15)

Data label	$R$	Parameters of NASGRO (H-S)				Parameters of model					
		$\Delta K_{thr}$	$A$	$C$	$m$	$k_1$	$k_2$	$10^{f_1}$	$f_2$	$f_3$	$f_4$
1	-0.2, 0.1, 0.4, 0.7, 0.8	4.02	87.3	$2.79 \times 10^{-10}$	2.12	4.02	87.30	$2.79 \times 10^{-10}$	2.12	2.12	-1.06
2	0.2, 0.4, 0.6	3.65	76.0	$2.79 \times 10^{-10}$	2.12	3.65	76.00	$2.79 \times 10^{-10}$	2.12	2.12	-1.06
3	0.1, 0.7	1.52	61.1	$2.79 \times 10^{-10}$	2.12	1.52	61.10	$2.79 \times 10^{-10}$	2.12	2.12	-1.06
4	-1.0, 0.01, 0.1, 0.3, 0.6	3.0	62.0	$1.52 \times 10^{-10}$	1.64	3.00	62.00	$1.52 \times 10^{-10}$	1.64	1.64	-0.82
5	0.2, 0.3, 0.6	3.59	57.0	$3.31 \times 10^{-10}$	2.42	3.59	57.00	$3.31 \times 10^{-10}$	2.42	2.42	-1.21

**Table A5** Experimental datasets used and the influencing factors reflected in the FAA's database

Label	Alloy type	Heat Treatment	Crack orientation	Test environments	Load ratios	Frequency, Hz
1	2014Al	T6	T-L	Laboratory air	0.05, 0.25, 0.38, 0.4, 0.5	2-30
2	2024Al	T3	L-T	Laboratory air	-2, -1, -0.5, 0.0, 0.5, 0.7	5-15
3	2024Al	T3	T-L	Laboratory air	0.0, 0.05, 0.33, 0.4, 0.7, 0.8	5-15
4	2024Al	T351	L-T	Laboratory air (different temperature)	-1, -0.5, 0.1, 0.4, 0.8	3-30
5	2024Al	T3511	L-T	Laboratory air, high-humidity air	0.05, 0.1, 0.5, 0.8	9-20
6	2024Al	T62	L-T	Laboratory air, high-humidity air, A/C sump water	0.1, 0.385, 0.7	0.1-30
7	2024Al	T81	L-T	Laboratory air, dry air	0.08, 0.1, 0.3, 0.5, 0.765	1-25
8	7050Al	T7451	L-T	Laboratory air, dry air	0.08, 0.1, 0.4, 0.5, 0.7, 0.8	6-50
9	7075Al	T651	L-T	Laboratory air	0.02, 0.1, 0.33, 0.5, 0.75	0.1-30
10	7075Al	T7351	L-T	Laboratory air, high-humidity air	-1, 0.1, 0.33, 0.5, 0.8	0.1-40
11	7475Al	T7351	L-T	Laboratory air	-3.33, -1, -0.33, 0.05, 0.1, 0.4, 0.8	1-20
12	7475Al	T761	L-T	Laboratory air, high-humidity air	0.05, 0.1, 0.25, 0.38, 0.8	2-30
13	7475Al	T7651	L-T	Laboratory air	0.0, 0.05, 0.4, 0.8	5-30

**Table A6** Parameters obtained by fitting the ParaGRO model to 13 datasets

Data label	$k_1$	$k_2$	$f_1$	$f_2$	$f_3$
1	3.4627	8.8376	-8.8463	6.1832	-2.6574
2	1.9101	5.5323	-8.3753	6.7391	-3.1795
3	1.6937	10.4839	-7.9658	5.2371	-1.7148
4	3.2265	12.8862	-8.8763	6.9000	-3.1389
5	1.7901	7.1824	-8.7380	7.3960	-3.0716
6	1.9434	5.4609	-8.0953	7.4630	-4.0347
7	5.5555	17.7690	-9.7765	6.7545	-2.8630
8	1.6451	6.7329	-8.0383	7.1368	-3.3948
9	2.7190	9.3176	-8.4711	6.5078	-2.8096
10	3.4112	11.8275	-8.3878	5.8223	-2.6225
11	1.8767	7.6002	-7.8736	6.3928	-2.9721
12	1.9346	7.0611	-7.5801	4.9275	-2.0541
13	9.3728	44.0707	-9.2636	5.2961	-2.0254

**Table A7** NASGRO model parameters used for 13 datasets (all other parameters are the same, with  $(S_{\max}/\sigma_0) = 0.3$ ,  $\alpha = 2.0$ ,  $a_0 = 0.0$ ,  $C_{\text{th}}^m = 0.1$ )

Data label	R	$K_{Ic}$	$\sigma_{YS}$	$A_k$	$B_k$	t	$\Delta K_1$	$C_{\text{th}}^p$	p	q	$\log_{10} C$	m
1	+	20	63	1.00	1.50	0.063	0.77	2.20	0.50	0.50	-7.64	3.0
2	+	30	53	1.00	1.50	0.100	1.22	1.21	0.25	1.00	-8.10	3.2
2	-	30	53	1.00	1.50	0.100	1.22	1.21	0.25	1.00	-8.10	3.2
3	+	27	48	1.00	1.50	0.090	1.00	1.50	0.25	1.00	-7.89	3.0
4	+	36	54	1.00	2.00	0.200	0.80	2.20	0.50	1.00	-8.40	3.6
4	-	36	54	1.00	2.00	0.220	0.80	2.20	0.50	1.00	-8.40	3.6
5	+	35	55	1.00	1.00	0.250	1.00	2.50	0.50	1.00	-8.40	3.5
6	+	38	58	1.00	1.00	0.125	0.82	2.20	1.00	1.00	-7.82	3.0
7	+	22	63	1.00	1.20	0.100	0.79	2.20	0.25	0.50	-8.15	3.3
8	+	32	73	1.00	0.75	0.500	0.80	2.20	1.00	1.00	-7.60	2.5
9	+	28	75	0.75	2.00	0.450	0.70	1.30	0.50	1.00	-7.52	2.8
10	+	32	63	1.00	1.00	0.400	0.70	2.00	0.50	0.50	-7.66	2.9
11	+	40	61	1.00	2.00	0.300	0.70	2.40	0.50	1.00	-7.40	2.6
11	-	40	61	1.00	2.00	0.300	0.70	2.40	0.50	1.00	-7.40	2.6
12	+	40	63	1.00	1.20	0.100	0.60	1.50	1.00	1.00	-7.30	2.4
13	+	40	69	1.00	1.50	0.200	0.64	2.15	0.50	1.00	-7.70	2.8

## Appendix B: NASGRO Model

$$\frac{da}{dN} = C(\Delta K)^m \left( \frac{1-f}{1-R} \right)^m \frac{\left( 1 - \frac{\Delta K_{\text{th}}}{\Delta K} \right)^p}{\left( 1 - \frac{K_{\max}}{K_c} \right)^q}$$

where

$$f = \frac{K_{\text{op}}}{K_{\max}} = \begin{cases} \max(R, A_0 + A_1 R + A_2 R^2 + A_3 R^3) & R \geq 0 \\ A_0 + A_1 R & -2 \leq R < 0 \\ A_0 - 2A_1 & R < -2 \end{cases}$$

$$\begin{cases} A_0 = (0.825 - 0.34\alpha + 0.05\alpha^2) \left[ \cos \left( \frac{\pi S_{\max}}{2\sigma_0} \right) \right]^{\frac{1}{\alpha}} \\ A_1 = (0.415 - 0.071\alpha) \frac{S_{\max}}{\sigma_0} \\ A_2 = 1 - A_0 - A_1 - A_3 \\ A_3 = 2A_0 + A_1 - 1 \end{cases}$$

$$\Delta K_{\text{th}} = \begin{cases} \Delta K_1 \left( \frac{a}{a+a_0} \right)^{\frac{1}{2}} \frac{\left( \frac{1-R}{1-f} \right)^{(1+RC_{\text{th}}^p)}}{(1-A_0)(1-R)C_{\text{th}}^p} & R \geq 0 \\ \Delta K_1 \left( \frac{a}{a+a_0} \right)^{\frac{1}{2}} \frac{\left( \frac{1-R}{1-f} \right)^{(1+RC_{\text{th}}^m)}}{(1-A_0)(C_{\text{th}}^p - RC_{\text{th}}^m)} & R < 0 \end{cases}$$

$$K_c = K_{Ic} \left\{ 1 + B_k e^{- \left[ A_k \frac{t}{2.5 \left( \frac{K_{Ic}}{\sigma_{YS}} \right)^2} \right]^2} \right\}$$

## Acknowledgments

The work was supported by the National Natural Science Foundation of China–Joint Fund of Civil Aviation Research (Grant

No. U2433213) and the National Natural Science Foundation of China (Grant No. 52402510). The second author was supported by the China Postdoctoral Science Foundation under Grant Nos. 2025T181120, 2025M774242.

## References

- [1] Wanhill, R., Molent, L., Barter, S., and Amsterdam, E., “Milestone Case Histories in Aircraft Structural Integrity,” National Aerospace Lab. TP 2015-193, Amsterdam, The Netherlands, Sept. 2015.
- [2] Paris, P. C., Gomez, M. P., and Anderson, W. E., “A Rational Analytic Theory of Fatigue,” *Trend in Engineering*, Vol. 13, 1961, pp. 9–14.
- [3] Paris, P., and Erdogan, F., “A Critical Analysis of Crack Propagation Laws,” *Journal of Basic Engineering*, Vol. 85, No. 4, 1963, pp. 528–533. <https://doi.org/10.1115/1.3656900>
- [4] Wood, H. A., and Engle, R. M., “USAF Damage Tolerant Design Handbook: Guidelines for the Analysis and Design of Damage Tolerant Aircraft Structures. Revision A,” Air Force Flight Dynamics Lab. TR 79-3021, Wright-Patterson AFB, OH, March 1979.
- [5] Forman, R. G., Kearney, V. E., and Engle, R. M., “Numerical Analysis of Crack Propagation in Cyclic-Loaded Structures,” *Journal of Basic Engineering*, Vol. 89, No. 3, 1967, pp. 459–463. <https://doi.org/10.1115/1.3609637>
- [6] Priddle, E. K., “High Cycle Fatigue Crack Propagation under Random and Constant Amplitude Loadings,” *International Journal of Pressure Vessels and Piping*, Vol. 4, No. 2, 1976, pp. 89–118. [https://doi.org/10.1016/0308-0161\(76\)90014-4](https://doi.org/10.1016/0308-0161(76)90014-4)
- [7] Elber, W., “The Significance of Fatigue Crack Closure,” *Damage Tolerance in Aircraft Structures*, edited by M. Rosenfeld, American Soc. for Testing and Materials, West Conshohocken, PA, 1971, pp. 230–242.
- [8] Gallagher, J. P., “A Generalized Development of Yield Zone Models,” Air Force Flight Dynamics Lab. TM FBR-74-28, Wright-Patterson Air Force Base, OH, Jan. 1974.
- [9] Hartman, A., and Schijve, J., “The Effects of Environment and Load Frequency on the Crack Propagation Law for Macro Fatigue Crack Growth in Aluminium Alloys,” *Engineering Fracture Mechanics*, Vol. 1, No. 4, 1970, pp. 615–631. [https://doi.org/10.1016/0013-7944\(70\)90003-2](https://doi.org/10.1016/0013-7944(70)90003-2)
- [10] Newman, J. C., and Raju, I. S., “Prediction of Fatigue Crack-Growth Patterns and Lives in Three-Dimensional Cracked Bodies,” *Fracture 84*, edited by S. R. Valluri, D. M. R. Taplin, P. R. Rao, J. F. Knott, and R. Dubey, Vol. 3, Pergamon, New Delhi, India, 1984, pp. 1597–1608.
- [11] Schijve, J., “Fatigue Crack Closure: Observations and Technical Significance,” *Mechanics of Fatigue Crack Closure*, edited by J. C. Newman, and W. Elber, American Soc. for Testing and Materials, West Conshohocken, PA, 1988, pp. 5–34.

- [12] Vaughan, R. E., and Chang, J. H., "Life Predictions for High Cycle Dynamic Components Using Damage Tolerance," *Journal of the American Helicopter Society*, Vol. 49, No. 4, 2004, pp. 493–500. <https://doi.org/10.4050/JAHS.49.493>
- [13] Maierhofer, J., Pippin, R., and Gänser, H.-P., "Modified NASGRO Equation for Physically Short Cracks," *International Journal of Fatigue*, Vol. 59, 2014, pp. 200–207. <https://doi.org/10.1016/j.ijfatigue.2013.08.019>
- [14] Forman, R. G., and Mettu, S. R., "Behavior of Surface and Corner Cracks Subjected to Tensile and Bending Loads in Ti-6Al-4V Alloy," NASA TM 102165, 1990.
- [15] Udrescu, S.-M., and Tegmark, M., "AI Feynman: A Physics-Inspired Method for Symbolic Regression," *Science Advances*, Vol. 6, No. 16, 2020, Paper eaay2631. <https://doi.org/10.1126/sciadv.aay2631>
- [16] Champion, K., Lusch, B., Kutz, J. N., and Brunton, S. L., "Data-Driven Discovery of Coordinates and Governing Equations," *National Academy of Sciences of the United States of America*, Vol. 116, No. 45, 2019, pp. 22,445–22,451. <https://doi.org/10.1073/pnas.1906995116>
- [17] Schmidt, M., and Lipson, H., "Distilling Free-Form Natural Laws from Experimental Data," *Science*, Vol. 324, No. 5923, 2009, pp. 81–85. <https://doi.org/10.1126/science.1165893>
- [18] Chen, Z., Liu, Y., and Sun, H., "Physics-Informed Learning of Governing Equations from Scarce Data," *Nature Communications*, Vol. 12, No. 1, 2021, p. 6136. <https://doi.org/10.1038/s41467-021-26434-1>
- [19] Flaschel, M., Kumar, S., and De Lorenzis, L., "Discovering Plasticity Models Without Stress Data," *npj Computational Materials*, Vol. 8, No. 1, 2022, p. 91. <https://doi.org/10.1038/s41524-022-00752-4>
- [20] Weng, B., Song, Z., Zhu, R., Yan, Q., Sun, Q., Grice, C. G., Yan, Y., and Yin, W.-J., "Simple Descriptor Derived from Symbolic Regression Accelerating the Discovery of New Perovskite Catalysts," *Nature Communications*, Vol. 11, No. 1, 2020, p. 3513. <https://doi.org/10.1038/s41467-020-17263-9>
- [21] Jung, H., "Machine-Guided Path Sampling to Discover Mechanisms of Molecular Self-Organization," *Nature Computational Science*, Vol. 3, No. 4, 2023, pp. 334–345. <https://doi.org/10.1038/s43588-023-00428-z>
- [22] Ma, H., Narayanaswamy, A., Riley, P., and Li, L., "Evolving Symbolic Density Functionals," *Science Advances*, Vol. 8, No. 36, 2022, Paper eabq0279. <https://doi.org/10.1126/sciadv.abq0279>
- [23] Rovinelli, A., Sangid, M. D., Proudhon, H., and Ludwig, W., "Using Machine Learning and a Data-Driven Approach to Identify the Small Fatigue Crack Driving Force in Polycrystalline Materials," *npj Computational Materials*, Vol. 4, No. 1, 2018, p. 35. <https://doi.org/10.1038/s41524-018-0094-7>
- [24] Garbrecht, K., Birky, D., Lester, B., Emery, J., and Hochhalter, J., "Complementing a Continuum Thermodynamic Approach to Constitutive Modeling with Symbolic Regression," *Journal of the Mechanics and Physics of Solids*, Vol. 181, 2023, Paper 105472. <https://doi.org/10.1016/j.jmps.2023.105472>
- [25] Zhou, S., Yang, B., Xiao, S., Yang, G., and Zhu, T., "Crack Growth Rate Model Derived from Domain Knowledge-Guided Symbolic Regression," *Chinese Journal of Mechanical Engineering*, Vol. 36, No. 1, 2023, p. 40. <https://doi.org/10.1186/s10033-023-00876-8>
- [26] Wu, C., Zhang, S., and Zhang, Y., "Development of a Generalizable Data-Driven Turbulence Model: Conditioned Field Inversion and Symbolic Regression," *AIAA Journal*, Vol. 63, No. 2, 2024, pp. 687–706. <https://doi.org/10.2514/1.J064416>
- [27] Geyer, T. F., and Enghardt, L., "Empirical Turbulence Interaction Noise Model for Permeable Flat Plate Leading Edges," *AIAA Journal*, Vol. 62, No. 6, 2024, pp. 2161–2173. <https://doi.org/10.2514/1.J063411>
- [28] Gan, L., Wu, H., and Zhong, Z., "Integration of Symbolic Regression and Domain Knowledge for Interpretable Modeling of Remaining Fatigue Life under Multistep Loading," *International Journal of Fatigue*, Vol. 161, 2022, Paper 106889. <https://doi.org/10.1016/j.ijfatigue.2022.106889>
- [29] Searson, D. P., "GPTIPS 2: An Open-Source Software Platform for Symbolic Data Mining," *Handbook of Genetic Programming Applications*, edited by A. H. Gandomi, A. H. Alavi, and C. Ryan, Springer-Verlag, Berlin, 2015, pp. 551–573.
- [30] O'Neill, M., Poli, Riccardo, Langdon, William B., and Nicholas, F., "McPhee: A Field Guide to Genetic Programming," *Genetic Programming and Evolvable Machines*, Vol. 10, No. 2, 2009, pp. 229–230. <https://doi.org/10.1007/s10710-008-9073-y>
- [31] Jones, R., Raman, R. K. S., Iliopoulos, A. P., Michopoulos, J. G., Phan, N., and Peng, D., "Additively Manufactured Ti-6Al-4V Replacement Parts for Military Aircraft," *International Journal of Fatigue*, Vol. 124, 2019, pp. 227–235. <https://doi.org/10.1016/j.ijfatigue.2019.02.041>
- [32] Jones, R., Kovarik, O., Bagherifard, S., Cizek, J., and Lang, J., "Damage Tolerance Assessment of AM 304L and Cold Spray Fabricated 316L Steels and Its Implications for Attributable Aircraft," *Engineering Fracture Mechanics*, Vol. 254, 2021, Paper 107916. <https://doi.org/10.1016/j.engfracmech.2021.107916>
- [33] Jones, R., Michopoulos, J. G., Iliopoulos, A. P., Singh Raman, R. K., Phan, N., and Nguyen, T., "Representing Crack Growth in Additively Manufactured Ti-6Al-4V," *International Journal of Fatigue*, Vol. 116, 2018, pp. 610–622. <https://doi.org/10.1016/j.ijfatigue.2018.07.019>
- [34] Forman, R. G., Shivakumar, V., Cardinal, J. W., Williams, L. C., and McKeighan, P. C., "Fatigue Crack Growth Database for Damage Tolerance Analysis," Federal Aviation Administration TR PB2005-110675, Washington, D.C., Aug. 2005.
- [35] Zhao, F., Zhou, X., Wang, C., Dong, L., and Atluri, S. N., "Setting Adaptive Inspection Intervals in Helicopter Components, Based on a Digital Twin," *AIAA Journal*, Vol. 61, No. 6, 2023, pp. 2675–2688. <https://doi.org/10.2514/1.J062222>

R. Ohayon  
Associate Editor